A. Romero-Calvo, A.J. Garcia-Salcedo, F. Garrone, I. Rivoalen, G. Cano-Gomez, E. Castro-Hernandez, F. Maggi
Free Surface Reconstruction of Opaque Liquids in Microgravity, Part 1: Design and On-Ground Testing
Acta Astronautica, Vol. 189, 2021, p. 250-259
doi:10.1016/j.actaastro.2021.08.029

Free surface reconstruction of opaque liquids in microgravity. Part 1: design and on-ground testing

Á. Romero-Calvo[a,b,*], A. J. García-Salcedo[b], F. Garrone[b], I. Rivoalen[b], G. Cano-Gómez[c], E. Castro-Hernández[d] and F. Maggi[b]

[a]Department of Aerospace Engineering Sciences, University of Colorado Boulder, CO, United States
[b]Space Propulsion Laboratory, Department of Aerospace Science and Technology, Politecnico di Milano, Via Giuseppe La Masa, 34, 20156, Milan, Italy
[c]Departamento de Física Aplicada III, Universidad de Sevilla, Avenida de los Descubrimientos s/n, 41092, Sevilla, Spain
[d]Departamento de Ingeniería Aeroespacial y Mecánica de Fluidos, Universidad de Sevilla, Avenida de los Descubrimientos s/n, 41092, Sevilla, Spain

ARTICLE INFO

Keywords:
Liquid interface
3D reconstruction
Microgravity
Ferrofluids
Magnetic liquid sloshing

ABSTRACT

This paper describes an inexpensive, non-invasive and highly adaptable surface reconstruction device for opaque liquids. The instrument was developed to study the lateral sloshing of ferrofluids in microgravity as part of the UNOOSA DropTES 2019 StELIUM project. Its design is driven by the geometrical and mechanical constraints imposed by ZARM's drop tower, where the experiment was launched in November 2019. The launch catapult and deceleration systems impose strong axial g-loads to a system that is confined in the reduced capsule environment. Redundant procedures are implemented to measure the first two lateral sloshing frequencies and damping ratios of the magnetic liquid, as well as its equilibrium surface in microgravity. Ideal vertical resolutions between 0.25 and 0.4 mm/px can be achieved with the configuration here proposed. The final performance depends, among other factors, on the correct application of the robust calibration procedure that is documented in this work.

1. Introduction

The term sloshing refers to the forced movement of liquids in partially filled containers [1]. The understanding of this phenomenon is of great importance for space vehicles, whose stability may be compromised by the chaotic motion of propellants in low-gravity environments [2]. Therefore, the experimental characterization of low-gravity liquid sloshing is a key step for the validation of theoretical models and technological development.

Several kinds of liquid level measurement techniques have been traditionally employed in liquid sloshing research. Those include displacement sensors such as linear potentiometers [3], laser beams [4, 5], capacitive probes [6], pressure transducers [7], or dynamometers [8], which produce an electric signal proportional to the movement. Lateral cameras are widely used to observe the lateral sloshing wave [9–12], sometimes with the scope of performing qualitative comparison with numerical predictions [13–15]. Liquid velocity profiles can also be obtained with the ultrasonic Doppler shift method [16]. The technique was used for measuring the sloshing of ferrofluids by Sawada [5, 17], who also employed the vertical displacement measurements of a sensor with the aim of analyzing the swirling phenomenon. Although these approaches are appropriate for many applications, the three-dimensional nature of sloshing sometimes requires more powerful alternatives.

The increase of computational power and the advancement of digital video recording technology has given rise to novel optical methods. Liquid level measurements can be obtained by processing the images of a float [18] or a pointer laser distortion in the liquid surface [19]. The surface can also be used as a mirror in order to compare an original and mirrored image in what is known as pattern fringe reflectometry [20, 21]. Alternatively, the distortion of a pattern behind the liquid can be employed [22, 23], an approach that has been addressed with deep neural networks in modern works [24]. Particle image velocimetry makes use of the motion of seeding particles in the fluid [25, 26]. In stereo imaging, the liquid surface and underwater scene are recorded by an array of cameras and then reconstructed [27]. Digital image correlation compares the frames of two cameras that record speckle particles in the liquid [28, 29].

Magnetic fields can be used to control liquid sloshing if the fluid responds to such stimulus [30]. This approach, known as *Magnetic Positive Positioning*, has been explored in the past for cryogenic propellants [12, 31, 32] and can be also employed to adjust the frequencies and damping ratios of a fluid system [33]. In the framework of the UNOOSA DropTES programme, the StELIUM (Sloshing of magnEtic LIqUids in Microgravity) microgravity experiment was launched at ZARM's drop tower in November 2019. The experiment studied the axisymmetric and lateral oscillations of a ferrofluid solution subjected to an inhomogeneous magnetic field in microgravity [34]. Most of the aforementioned liquid level measurement methods require expensive hardware components, complex post-processing, large and delicate setups, transparent liquids, or direct contact with the fluid. An alternative sloshing detection system was then required for this experiment, whose design was highly conditioned by the magnetic and opaque nature of ferrofluids and the overwhelming role of surface tension in low-gravity environments. In addition, the experiment setups used in drop tower experiments must be compact, autonomous, highly resistant to impacts,

*alvaro.romerocalvo@colorado.edu
ORCID(s): 0000-0003-3369-8460 (Á. Romero-Calvo)

Nomenclature

α	Magnification in x
a_i	Intrinsic coefficients for omnidirectional cameras
β	Magnification in y
γ	Container tilting angle
$\overline{\gamma}_k$	Experimental container tilting angle in the k axis
c	Stretching parameter for omnidirectional cameras
$\mathbf{d} = \{\mathrm{d}_x, \mathrm{d}_y, \mathrm{d}_z\}^T$	Position of the laser projection with respect to the laser pointer
d	Module of $\mathbf{d}$
e	Stretching parameter for omnidirectional cameras
f	Focal length
g	Liquid surface shape function
h_0	Height over horizontal surface line
k	Pixel density in x
k_i	Coefficients of radial distortion
λ	Scaling factor of the position vector $\mathbf{P}_C$
$\mathbf{l} = \{\mathrm{l}_x, \mathrm{l}_y, \mathrm{l}_z\}^T$	Position of the laser with respect to the focal point
l	Pixel density in y
$\mathcal{M}$	Matrix of intrinsics for standard camera
m	Stretching parameter for omnidirectional cameras
$\hat{\mathbf{n}} = \{\hat{\mathrm{n}}_x, \hat{\mathrm{n}}_y, \hat{\mathrm{n}}_z\}^T$	Unitary vector perpendicular to the laser plane
ω	Free surface oscillation frequency
P_C	Module of $\mathbf{P}_C$
$\mathbf{P}_C = \{X_c, Y_c, Z_c\}^T$	Camera-attached coordinates
$\mathbf{P}_W = \{X, Y, Z\}^T$	World coordinates
$\mathbf{p}_d = \{x, y\}^T$	Distorted pixel coordinates
$\mathbf{p}_u = \{x', y'\}^T$	Undistorted pixel coordinates
p_i	Coefficients of tangential distortion
p_{ij}	Surface function fitting coefficients
$\mathcal{Q}$	First stretching matrix for omnidirectional cameras
$\mathbb{R}^n$	Real space with dimension n
$\mathcal{R}$	Rotation matrix
$\mathbf{r}$	Position of the laser point with respect to the focal point
r'	Radius of undistorted image coordinates
r_n	Normalized radius of undistorted image coordinates
r	Module of $\mathbf{r}$
s	Radius in centered image coordinates
$\mathcal{T}$	Extrinsic matrix transformation
θ	Angle between image axes
$\boldsymbol{t}$	Translation vector
x_0	Coordinate x of the optical center
x'_{n}	Normalized undistorted image coordinate in x
y_0	Coordinate y of the optical center
y'_{n}	Normalized undistorted image coordinate in y
$\square^T$	Transpose operator
$\hat{\square}$	Unit vector

and reliable.

The Sloshing Detection Subsystem (SDS) of StELIUM is an inexpensive, non-invasive and highly adaptable device designed to: (i) reconstruct the free surface of the magnetic liquid, (ii) study the first two sloshing frequencies and modal shapes of the oscillation, and (iii) compute their corresponding damping ratios. The theoretical modeling of the system is given in Sec. 2, with the hardware and software being described in Sec. 3. On-ground results are presented in Sec. 4, and relevant conclusions are extracted in Sec. 5.

2. Theoretical framework

2.1. Geometric camera calibration

The terms *geometric camera calibration* or *camera resectioning* refer to the determination of the parameters that correlate the position of a world point with its representation in the image plane of a particular camera. Those parameters include the focal length, size of the pixels, position of the image center and the rigid-body position of the camera, among others [35]. The link is generally established by means of the three step procedure represented in Fig. 1: (i) rigid transformation from world coordinates $\mathbf{P}_W = \{X, Y, Z\}^T$ to camera-attached coordinates $\mathbf{P}_C = \{X_c, Y_c, Z_c\}^T$ (*extrinsic parameters*), with ^{T} denoting the transpose operator, (ii) projective transformation from camera-attached coordinates to undistorted pixel coordinates in the retinal (or image) reference system $\mathbf{p}_u = \{x', y'\}^T$ (*intrinsic parameters*), and (iii) radial and tangential distortion from undistorted to distorted pixel coordinates $\mathbf{p}_d = \{x, y\}^T$ (*distortion parameters*), also expressed in the retinal frame. With this nomenclature, uppercase and lowercase letters denote the physical and image frames, respectively. As shown in Fig. 1, the origins of the world, camera-attached, and retinal reference systems are located at an arbitrary world point, the pinhole, and the upper left corner of the image, respectively.

From now on, *homogeneous coordinates* are employed, which transform a vector with dimensions $\mathbb{R}^n$ into a $\mathbb{R}^{n+1}$ space by adding an additional component equal to 1. The world point $\mathbf{P}_W$ and distorted pixel coordinates $\mathbf{p}_d$ are then

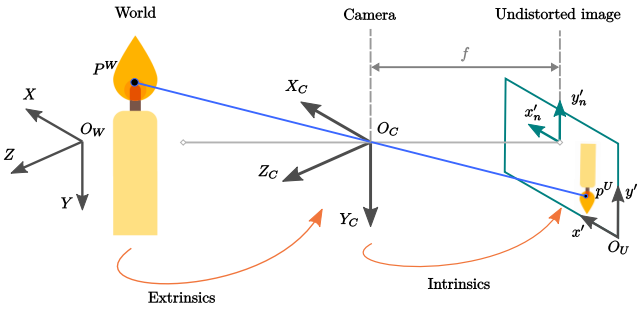

Figure 1: Camera calibration procedure. World (W), camera-attached (C) and retinal (U) reference systems have been represented.

represented in the homogeneous space by $\{X, Y, Z, 1\}^T$ and $\{x, y, 1\}^T$, respectively. This enables a compact matrix representation of the geometric transformations.

2.1.1. *Extrinsic parameters*

The transformation between world and camera-attached reference systems is represented by a 3×3 rotation matrix $\mathcal{R}$ and a translation vector $\boldsymbol{t} \in \mathbb{R}^3$, expressed in homogeneous coordinates as [35]

$$\mathbf{P}_C = \mathcal{T}\mathbf{P}_W, \quad \text{where} \quad \mathcal{T} = \begin{bmatrix} \mathcal{R} & \boldsymbol{t} \\ \mathbf{0}^T & 1 \end{bmatrix}. \tag{1}$$

The extrinsic parameters give the position and orientation of the camera with respect to an external reference frame. This information is of particular interest for computer vision applications.

2.1.2. *Intrinsic parameters for standard cameras*

The transformation from camera-attached coordinates to undistorted pixel coordinates for standard cameras is defined by five intrinsic parameters: (i) the magnifications $\alpha = kf$ and $\beta = lf$, where k and l are, respectively, the pixel dimensions in the x and y axes [px/m], and f is the focal length [m], (ii) the angle θ between the image axes, which may deviate slightly from 90° due to manufacturing errors, and (iii) the position of the optical center $\{x_0, y_0\}$ [px] in the retinal reference system. Assuming that the camera is focused at infinity or, equivalently, that the distance between the pinhole and the sensor plane is equal to the focal length, these parameters are related through [35]

$$\mathbf{p}_u = \frac{1}{Z}\mathcal{M}\mathbf{P}_C, \quad \text{where} \quad \mathcal{M} = \begin{bmatrix} \alpha & -\alpha\cot\theta & x_0 & 0 \\ 0 & \frac{\beta}{\sin\theta} & y_0 & 0 \\ 0 & 0 & 1 & 0 \end{bmatrix}. \tag{2}$$

It should be noted that the undistorted pixel coordinates are referred to the retinal reference system and not to the optical center $\{x_0, y_0\}$.

The previous derivation has implicitly assumed a pinhole camera model. However, modern cameras usually implement a complex system of lenses that induce *radial* and *tangential* distortions in the images. The undistorted and distorted pixel coordinates can be related by means of [36]

$$\frac{x - x_0}{\alpha} = x'_{\mathrm{n}}(1+k_1 r_n^2+k_2 r_n^4+k_3 r_n^6)+2p_1 x'_{\mathrm{n}} y'_{\mathrm{n}}+p_2(r_n^2+2x'^2_{\mathrm{n}}), \tag{3}$$

$$\frac{y - y_0}{\beta} = y'_{\mathrm{n}}(1+k_1 r_n^2+k_2 r_n^4+k_3 r_n^6)+2p_2 x'_{\mathrm{n}} y'_{\mathrm{n}}+p_1(r_n^2+2y'^2_{\mathrm{n}}), \tag{4}$$

where k_i are the coefficients of radial distortion, p_i are the coefficients of tangential distortion, $r_n^2 = x'^2_{\mathrm{n}} + y'^2_{\mathrm{n}}$ is the normalized undistorted radius, and the dimensionless normalized image coordinates are defined as

$$x'_{\mathrm{n}} = \frac{x' - x_0}{\alpha}, \quad y'_{\mathrm{n}} = \frac{y' - y_0}{\beta}. \tag{5}$$

The distorted pixel coordinates $\mathbf{p}_d = \{x, y\}^T$ are expressed in the retinal frame. A dedicated calibration process has to be followed to obtain the distortion parameters for a specific camera.

2.1.3. *Intrinsic parameters for omnidirectional cameras*

Commercial action cameras with wide fields of view, like the GoPro Hero 5 Session employed in this work, usually induce strong image distortions (fisheye effect). Specific calibration procedures have been developed for them, one of the most popular being Scaramuzza's camera model [37]. The transformation from undistorted pixel coordinates to camera-attached coordinates is now expressed as

$$\begin{bmatrix} X_c \\ Y_c \\ Z_c \end{bmatrix} = \lambda \begin{bmatrix} x' - x_0 \\ y' - y_0 \\ a_0 + a_2 r'^2 + a_3 r'^3 + a_4 r'^4 \end{bmatrix}, \tag{6}$$

where λ is the scaling factor of the position vector $\mathbf{P}_C$, a_i are a series of fitting coefficients with $a_1 = 0$, and $r'^2 = (x' - x_0)^2 + (y' - y_0)^2$. The model accounts for stretching through

$$\mathbf{p}_d = \mathcal{Q}\mathbf{p}_u, \text{ where } \mathcal{Q} = \begin{bmatrix} c & e & (1-c)x_0 - ey_0 \\ m & 1 & -mx_0 \\ 0 & 0 & 1 \end{bmatrix}, \tag{7}$$

with c, e and m being the stretching parameters.

2.1.4. *Calibration process*

Several calibration algorithms with different degrees of autonomy and accuracy can be used to fit the extrinsic, intrinsic, and distortion parameters of the camera [38, 39]. In this work, the extrinsic parameters are estimated from geometrical measurements. Matlab's Camera Calibration Toolbox [40], that employs a checkerboard-based fitting process, is used to compute the intrinsics. The interested reader is

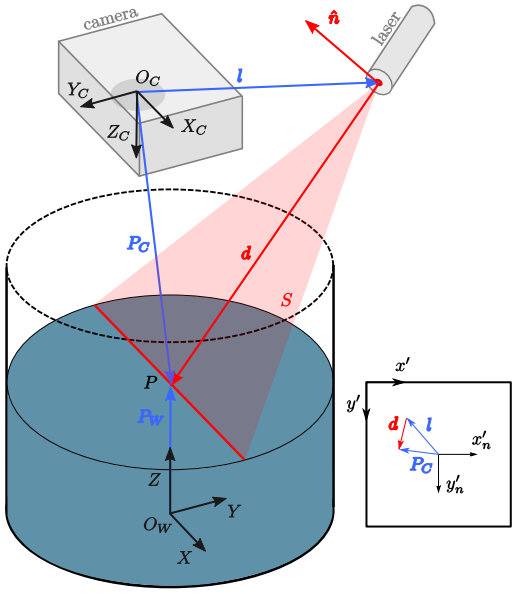

Figure 2: Minimum working example of the detection system

referred to the general description of the standard[1] and fisheye[2] calibration procedures implemented in the Matlab Single Camera Calibrator App[3] for further details.

2.2. Surface Reconstruction

In the proposed surface reconstruction system, a set of laser diodes and/or laser lines and a video camera with known position and orientation are directed towards the fluid surface. The movement of the opaque liquid is perceived by the camera as a displacement of the laser pattern projected over the surface. The observations are then correlated with the position of each laser point in the world coordinate frame.

A representative example consisting on a video camera and a laser line is first depicted in Fig. 2. The line is treated as a set of points, and so the discussion is focused on the reconstruction of point P. Since P is defined by the intersection of the laser position vector $\mathbf{d}$ and the visual line $\mathbf{P}_C$, the geometrical relation

$$\mathbf{P}_C = \mathbf{l} + \mathbf{d} \tag{8}$$

must be satisfied, with $\mathbf{l}$ being the position of the laser pointer in the camera-attached coordinate frame.

The unitary vector $\hat{\mathbf{P}}_C$, that defines the direction of the visual line, can be computed from the distorted pixel coordinates $\mathbf{p}_d$ by employing the intrinsic camera transformation. Assuming that $\mathbf{l}$ is known and that $\mathbf{d}$ is constrained by the position and orientation of the laser, the problem is reduced to the computation of $\mathbf{P}_C$ from the projection $\mathbf{p}_d$ in the retinal reference system. The world coordinates are finally obtained with the extrinsic transformation.

The solution procedure is dependent on the type of geometrical constraint that is applied to $\mathbf{d}$. The cases of a laser diode and a laser line are subsequently addressed.

[1] https://mathworks.com/help/vision/ug/camera-calibration.html Accessed on: 20/08/2020
[2] https://mathworks.com/help/vision/ug/fisheye-calibration-basics.html Accessed on: 20/08/2020
[3] https://mathworks.com/help/vision/ug/single-camera-calibrator-app.html Accessed on: 20/08/2020

2.2.1. *Laser diode*

If a laser pointer is employed, P remains in the line defined by the unitary vectors $\hat{\mathbf{d}}$ and $\hat{\mathbf{P}}_C$, and Eq. 8 becomes

$$\begin{bmatrix} \hat{X}_c & -\hat{\mathrm{d}}_x \\ \hat{Y}_c & -\hat{\mathrm{d}}_y \\ \hat{Z}_c & -\hat{\mathrm{d}}_z \end{bmatrix} \begin{bmatrix} \mathrm{P_C} \\ \mathrm{d} \end{bmatrix} = \begin{bmatrix} \mathrm{l}_x \\ \mathrm{l}_y \\ \mathrm{l}_z \end{bmatrix}, \tag{9}$$

which is an overdetermined system that can be solved by means of a weighted least-squares algorithm.

It should be noted that $\mathbf{l}$ and $\hat{\mathbf{d}}$ are assumed to be known beforehand. While the former is a design parameter, the latter usually needs to be determined experimentally. A possibility is to impose a liquid surface shape $Z = g(X, Y)$ and use a single camera picture to extract the position of the laser pointer in the retinal reference system, $\mathbf{p}_d$. The intrinsic transformation can then be used to compute the camera-attached coordinates and solve the system given by Eq. 9 for $\mathbf{d}$. This procedure can be reinforced by analyzing different $g(X, Y)$ surfaces and making use of a least-squares calibration.

2.2.2. *Laser line*

If the laser pointer is substituted by a laser line, the unitary vector $\hat{\mathbf{d}}$ is no longer fixed. However, it is still contained in the laser plane defined by the unitary normal vector $\hat{\mathbf{n}}$, assumed to be known, and must then satisfy the equation

$$\hat{\mathbf{n}} \cdot \hat{\mathbf{d}} = \mathbf{0}, \tag{10}$$

resulting in the square system

$$\begin{bmatrix} \hat{X}_c & -1 & 0 & 0 \\ \hat{Y}_c & 0 & -1 & 0 \\ \hat{Z}_c & 0 & 0 & -1 \\ 0 & \hat{\mathrm{n}}_x & \hat{\mathrm{n}}_y & \hat{\mathrm{n}}_z \end{bmatrix} \begin{bmatrix} \mathrm{P}_C \\ \hat{\mathrm{d}}_x \\ \hat{\mathrm{d}}_y \\ \hat{\mathrm{d}}_z \end{bmatrix} = \begin{bmatrix} \mathrm{l}_x \\ \mathrm{l}_y \\ \mathrm{l}_z \\ 0 \end{bmatrix}, \tag{11}$$

which, unlike the laser diode case, is not overdetermined.

3. Materials and methods

3.1. StELIUM experiment setup

The experiment setup of StELIUM, represented in Fig. 3, is designed to apply a lateral percussion to a partially filled container and measure its response in microgravity. The oscillation of the magnetic fluid is recorded by the SDS while subjected to the influence of a static magnetic field. All the scientific tasks must be completed within the 9.3 seconds of flight provided by ZARM's drop tower.

Two platforms hold identical assemblies of the experiment, which is placed inside a standard drop tower capsule [41]. Each assembly includes a Plexiglas container of 110 mm diameter and 200 mm height filled up to 50 mm with a 1:5 volume solution of the Ferrotec EMG-700 water-based ferrofluid. The container is surrounded by a coil of 94.25 mm nominal diameter with a width of 25 mm and 200 windings of a 1.8 mm copper wire. A constant current power source feeds the coils with intensities ranging from 0 to 20

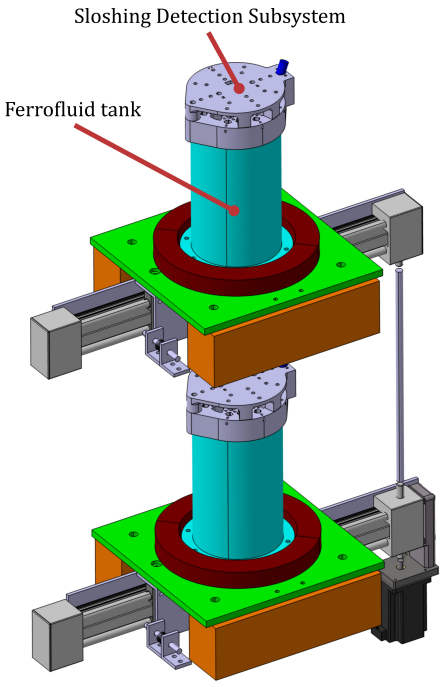

Figure 3: StELIUM experiment setup

A. Each assembly is actuated by a sliding mechanism fixed to the capsule platform, powered by a stepper engine, and connected by means of an aluminum shaft to its counterpart. A locking mechanism fixes the moving parts and prevents undesired displacements at the beginning and end of the drop. The total mass of the experiment, including the platforms, is approximately 60 Kg. The system has an overall volume of $930 \times 530 \times 295$ mm^3 [34].

3.2. High-level requirements of the Sloshing Detection Subsystem

The design of the SDS must satisfy the high level requirements listed in Tab. 1. It should be noted that the first three ones are related to the performance of the system, while the rest refer to its integrity and reliability as a component of the experiment setup.

3.3. Sloshing Detection Subsystem design

The SDSs are located over the ferrofluid containers. Their basic components are twenty laser pointers, a tilted line laser and a GoPro Hero 5 Session camera that records their apparent displacement. Those elements interact as described in Sec. 2.2 to reconstruct the free surface shape.

The SDS is mounted on a 3D printed PLA structure that holds the electronic components. Fig. 4 shows the bottom view of the SDS, which is adapted to the cylindrical vessel employed in the experiment and provides high structural resistance with a low mass penalty. Those characteristics are critical for withstanding the 50 g deceleration load of ZARM's drop tower.

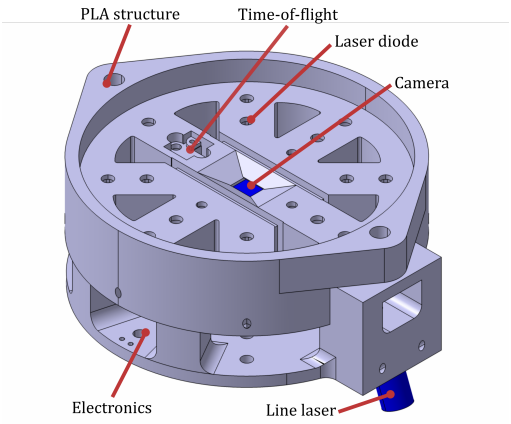

Figure 4: Bottom view of the Sloshing Detection Subsystem

A fast and low-cost development is achieved by selecting commercial off-the-shelf Arduino electronics. Those include an Arduino Mega board, two MOSFET transistors, an accelerometer, an SD Card reader, a laser time-of-flight sensor, a potentiometer, a set of 20 laser diodes and a line laser. The subsystem is powered by a 5V USB cable and is programmed before each drop to work autonomously. A single trigger line interfaces the SDS with the Capsule Control System. In this way, the pre-programmed automation routines can be launched when requested. The electrical connections among the different elements are described in Ref. [34].

The laser diodes are distributed in three concentric circular rings with radii corresponding to the theoretical peaks of the first three lateral sloshing modes in microgravity. This choice eases the measurement of higher order oscillations, whose amplitude is small in comparison with the fundamental wave. The diodes are encapsulated in a 3D-printed PLA holder that fixes their position and allows a precise focusing before operation. A small tilting of the laser beam is produced because of manufacturing errors, but is compensated by the calibration procedure. The line laser produces a single line at the fluid surface that crosses the center of the vessel. When the liquid reaches its equilibrium position in micro-

Table 1
High level requirements

ID	Requirement
1	The SDS shall be able to measure the fundamental lateral sloshing frequency and damping ratio of the liquid.
2	The SDS should be able to measure the second lateral sloshing frequency and damping ratio of the liquid.
3	The SDS shall be able to reconstruct the radial profile of the meniscus.
4	The SDS shall withstand at least 4 catapult drops.
5	The SDS shall operate autonomously.
6	The SDS shall implement redundant measurement techniques.

gravity, the deformation of the laser line unveils the shape of the meniscus. Besides, the laser line can also be employed to reconstruct the fluid surface if an almost-perfect lateral oscillation is produced and the line is aligned with the actuation. The two sets of lasers are regulated by their corresponding MOSFET transistors and a manual potentiometer.

The GoPro Hero 5 Session camera is placed at the center of the structure and is configured to work at 4K resolution and 30 fps speed. The resulting video measurements are processed as described in Sec. 2. Reflections can be mitigated with a neutral filter located over the lens. A Photron Fastcam MC2.1 camera working at 125 fps is used for lateral visualization, with both cameras being synchronized with the blink of a LED at the beginning of each drop.

This setup suffices the experiment requirements enumerated in Tab. 1. However, a complementary system is installed to record the fundamental sloshing frequency and the acceleration of the container. A VL53L0X time-of-flight sensor is used to measure the mean ferrofluid height in a region covering approximately half of the free surface. This measurement is used to quickly compute the fundamental oscillation frequency, an information that becomes useful for obtaining a quick feedback between drops. An MPU6050 accelerometer measures the acceleration of the ferrofluid container during the drop in the direction of the excitation. Both components are powered and controlled by the Arduino Mega board, that records acceleration and time-of-flight data in the SD card for later analysis.

3.3.1. Calibration of $\hat{\mathbf{d}}$ *and* $\hat{\mathbf{n}}$

The process for estimating $\hat{\mathbf{d}}$ described in Sec. 2.2 is implemented and tested. It is based on the following steps:

1. Measure (or estimate) the height h_0 and the position vector $\mathbf{l}$ of the laser pointers with respect to the axis of the camera.
2. Tilt the container an angle γ in the lateral axis in order to produce a surface of the form $g(x, y) = h_0 - x \tan\gamma$ or $g(x, y) = h_0 - y \tan\gamma$.
3. Take a short video with the desired camera configuration and extract a single frame.
4. Hand-pick the position of the laser points.
5. Run a centroid-location algorithm to refine the position of the laser points using the hand-picked value as an initial estimation.
6. For each point, a single observation $\{x, y\}^T$ is available. Since $\mathbf{l}$ and h_0 (or Z) are known, X and Y can be computed from Eqs. 6 and 7. $\hat{\mathbf{d}}$ is finally obtained from Eq. 8.

The procedure is illustrated for an horizontal calibration profile $g(x, y) = h_0$ in Fig. 5. The physical position of the laser diodes, which is know beforehand, is transformed to the retina reference system and represented by green crosses. These points diverge from the actual projections, which are marked as red circles, due to the small tilting of the laser diodes. The path followed by the points when the height of the surface oscillates between 1 and 10 cm is represented by a red line with an uniform discretization in Z. As the points get closer to the optical center the segments become smaller, reflecting a decrease in the vertical resolution.

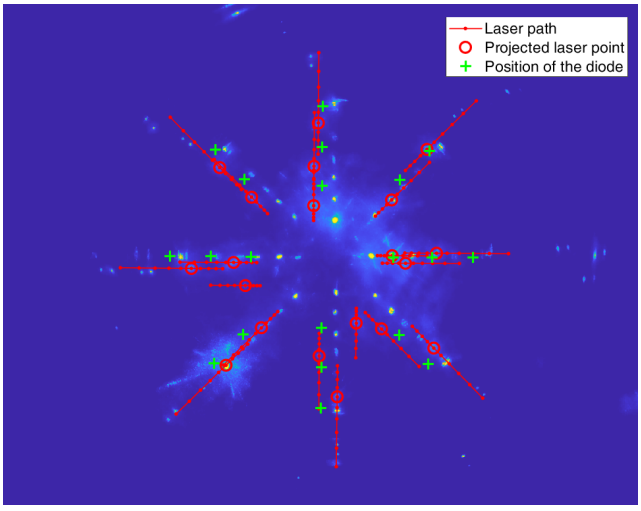

Figure 5: Results from the $\hat{\mathbf{d}}$ calibration process for an horizontal surface. The laser projections are surrounded by red circles, which differ slightly from the green crosses that show the position of the diodes in the detection head. The red lines represent the path of the diodes for heights between 1 and 10 cm. Additional yellow points correspond to secondary reflections in the walls of the container.

Since the projection of the laser line over the ferrofluid surface is a straight line, a much simpler calibration strategy is followed for $\hat{\mathbf{n}}$. First, the contact points with the edges of the free surface are clearly observable, which facilitates the selection of an appropriate configuration. Secondly, the tilting angle in the $\hat{\mathbf{n}}$-$\hat{\mathbf{d}}$ plane can be easily computed by knowing the position of the laser head and the laser line (again, obtained from the edges). Finally, the rotation around the axis of the laser can be adjusted to produce a flat surface (or, in low-gravity conditions, a balanced meniscus). Further details on the operation of the laser line can be found in the second part of this paper [42]

3.4. Surface reconstruction algorithm

If the value of $\mathbf{p}$ has been correctly estimated from video observations, the 3D reconstruction of the free surface based on a set of laser points only requires to:

1. Locate the position of the laser points in the initial video frame, where the surface shape $g(x, y)$ is assumed to be known.
2. Run the calibration algorithm to obtain $\hat{\mathbf{d}}$.
3. For each subsequent video frame, locate the new position of the laser point with a centroid-location algorithm. A Gaussian probability curve centered at the previous location with an appropriate standard deviation should be employed to avoid false-positives. Fast light reflections can be removed by means of a Hampel filter applied in the time domain with a window of 3 to 7 frames.

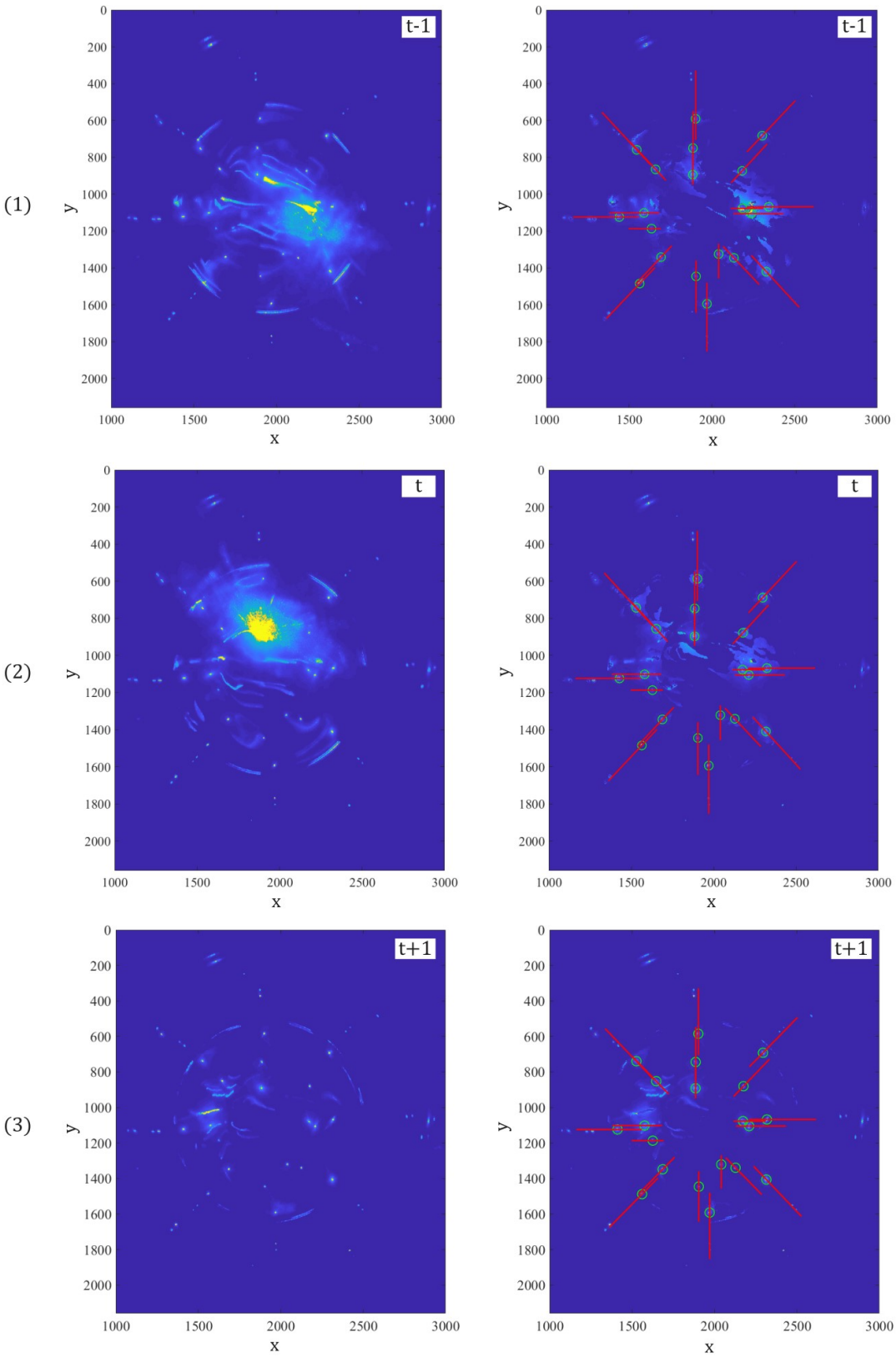

Figure 6: Sequence of three consecutive video frames at $t-1$ (a), t (2) and $t+1$ (3) showing the laser point location algorithm. The original images are displayed in column (a), while column (b) represents the result of the filtering process. The laser points are surrounded by a green circle and must remain in their red lines, that span between 1 and 10 cm height.

4. Compute the time-dependent position of each laser point as described in Sec. 2.2.
5. Extract relevant parameters of the three-dimensional surface evolution (e.g. modal shapes and frequencies, damping ratios, surface rotation, etc)

This procedure is exemplified in Fig. 6 for a sequence of three video frames on which a particularly strong laser reflection is produced. The original images are given in the left column, while the right one represents the result of applying a 5-frames Hampel filter. Green circles surround the laser points, which are determined by means of a centroid location algorithm. Their movement is always restricted to the red path represented in the image.

Laser reflections mask the actual laser points for a short time, hindering the centroid location process and inducing aberrations. Although during those events the position of the points is unknown, the Hampel filter and Gaussian tracking ease the recovering process and hence increase the robustness of the method. The artifacts produced by laser reflections appear in the final $\{X, Y, Z\}^T$ values as sharp steps, blank windows or detachments. The loss of tracking can be corrected with a fine tuning of the centroid tracking algorithm, but other aberrations are unavoidable. However, this has a very limited impact on the overall quality of the results.

A fully analogous process is followed for laser lines. The equations presented in Sec. 2.2.2 should be employed together with the calibration strategy described in Sec. 3.3.1. However, a condition of spatial continuity between adjacent points is also imposed, as described in the second part of this paper [42].

4. Results

4.1. GoPro Hero 5 Session intrinsics

The GoPro Hero 5 Session camera is calibrated with 19 checkerboard images as described in Sec. 2.1.4. The calibration parameters are given in Tab. 2 and resulted in an overall mean error of 0.25 px.

4.2. Ideal performance

The performance of the SDS will depend on its configuration, hardware selection and post-processing algorithms.

Table 2
GoPro Hero 5 Session calibration parameters

Parameter	Value	Errors	Unit
a_0	1722.6932	± 0.9879	-
a_2	-1.2637e-4	± 4.5193e-6	-
a_3	5.9090e-9	± 1.0902e-8	-
a_4	-1.0064e-11	± 7.0072e-12	-
c	0.9986	± 9.5856e-5	-
e	0.0012	± 4.8446e-4	-
f	-4.4337e-4	± 5.1676e-4	-
x_0	1926.6676	± 0.9946	px
y_0	1081.6723	± 1.2160	px

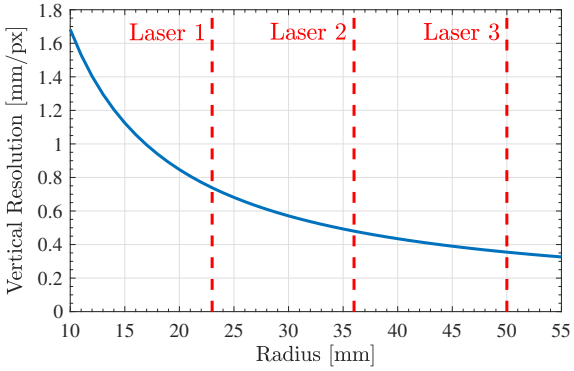

Figure 7: Ideal vertical resolution of the Sloshing Detection Subsystem as a function of the radius of separation l of the laser diode

The GoPro Hero 5 Session camera has a 3840×2160 px^2 resolution at 30 fps with an horizontal FOV of 118.9° and a vertical FOV of 69.7°. Since the camera is at approximately 17 cm from the flat ferrofluid surface, the 5.5 cm radius surface fits inside an image of 1470×1470 px^2. Assuming that the laser lines are perfectly vertical, the resolution of the system, defined as dx/dZ, can be computed from Eqs. 6 and 7. The result is presented in Fig. 7 as a function of the radius of separation of the laser diode (l). The dashed lines denote the radial position of the diodes in the structure of the SDS.

The same procedure can be employed to compute the vertical resolution of the line laser, which is tilted 20° with respect to the axis of symmetry. A value of approximately 0.27 mm/px is obtained, suggesting that significant improvements can be achieved with an appropriate geometrical configuration of the laser diodes.

4.3. Actual performance

From the theoretical viewpoint, the SDS should have a resolution of less than 0.5 mm/px in the external ring of laser pointers. The actual value is greater due to the uncertainties in the determination of $\mathbf{l}$ and $\hat{\mathbf{d}}$, the residual tilting of the camera and the errors induced by the image analysis algorithms. The previous theoretical calculations also assume that the position of the laser points can be obtained with pixel accuracy. However, each projection covers several pixels. Even if a centroid location algorithm is employed, the exact position of the center will be always subjected to uncertainty. Additional factors, such as mechanical vibrations (e.g. ZARM's drop tower catapult), thermal stability, or an inaccurate camera calibration, also have a negative effect on the performance.

In order to measure the overall static performance of the SDS, the $\hat{\mathbf{d}}$ vector is first estimated for different angles by following the procedure described in Sec. 3.3.1. A known tilting γ between 0° and 35° in the X axis with 0.5° accuracy is imposed to the ferrofluid container with the tilting table shown in Fig. 8. The Y axis, perpendicular to X and parallel to the surface, is kept close to 0°. The images corresponding to 0° and 30° are given in Fig. 9 for illustrative purposes. The

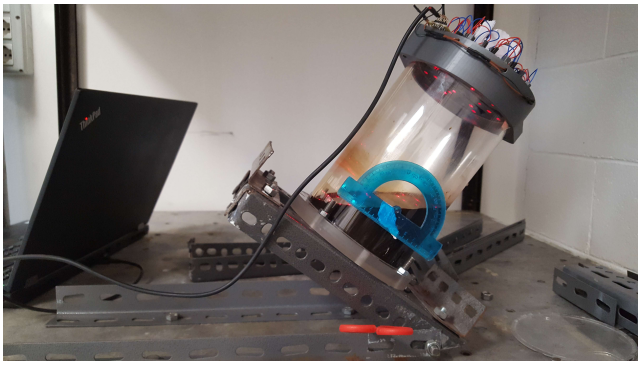

Figure 8: Calibration setup

first depicts many more points than lasers as a consequence of the reflections on the walls of the container. Since for the second case the reflected laser beams are not interfering with the surface, each point is clearly observed in the image. The resulting $\hat{\mathbf{d}}_i$ vectors are averaged and a mean value $\hat{\mathbf{d}}$ is obtained. The difference vector $\hat{\mathbf{d}}_i - \hat{\mathbf{d}}$ is computed for each case, resulting in a mean module of just $7.18 \cdot 10^{-4}$.

Once the values of $\hat{\mathbf{d}}$ are obtained, the corresponding $\{X, Y, Z\}^T$ points are fitted for each tilting angle with a function of the form

$$g(X, Y) = p_{00} + p_{10}X + p_{01}Y, \tag{12}$$

and the observed inclinations $\overline{\gamma}_X$ and $\overline{\gamma}_Y$ are compared with the ones imposed to the container. The result of the analysis is shown in Tab. 3. The R^2 value stays approximately constant and above 0.985 excluding the 0° case, but the Root Mean Square Errors (RMSEs) increase linearly from 0.2 to 2.4 mm with the tilting angle. In other words, the dispersion of the 20 punctual measurements remains constant in relative terms and increases in absolute terms. These values represent a good indicator of the performance of this particular system under different operation regimes. However, the linear increase in the RMSE with the tilting angle points to an error in the determination of the geometrical parameters of the system. The uncertainties in the height h_0 and orientation of the camera, which is assumed to be perpendicular to the horizontal fluid surface, may be behind this behavior.

The difference between $\overline{\gamma}_X$ and γ is close to 0°, but steps to more than 1.25° for the cases 6 to 8. $\overline{\gamma}_Y$ increases linearly from −0.19° to 5.06° while it should remain close to 0°. This may be explained by a misalignment between the actual X axis and the camera x axis. Again, these results highlight the importance of performing a correct estimation of the different parameters of the system.

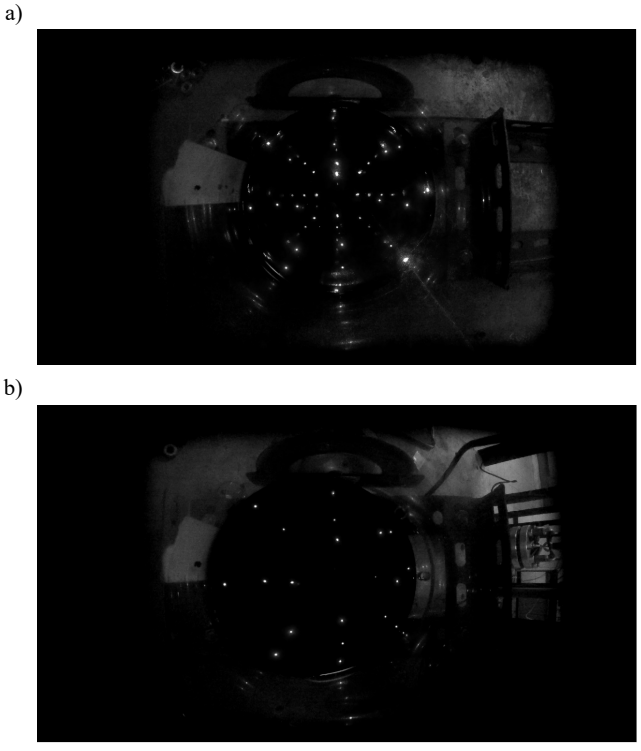

Figure 9: Video frames from the GoPro Hero 5 Session camera for: a) 0° and b) 30° tilting angles during a ground test.

4.4. Single-point operation

Although the SDS has been designed to reconstruct the free surface of the liquid, the displacement of a single laser diode in the retinal reference system can be used to compute the sloshing frequencies and approximate damping ratios. This is true even if the laser moves slightly due to the acceleration exerted by the drop tower catapult.

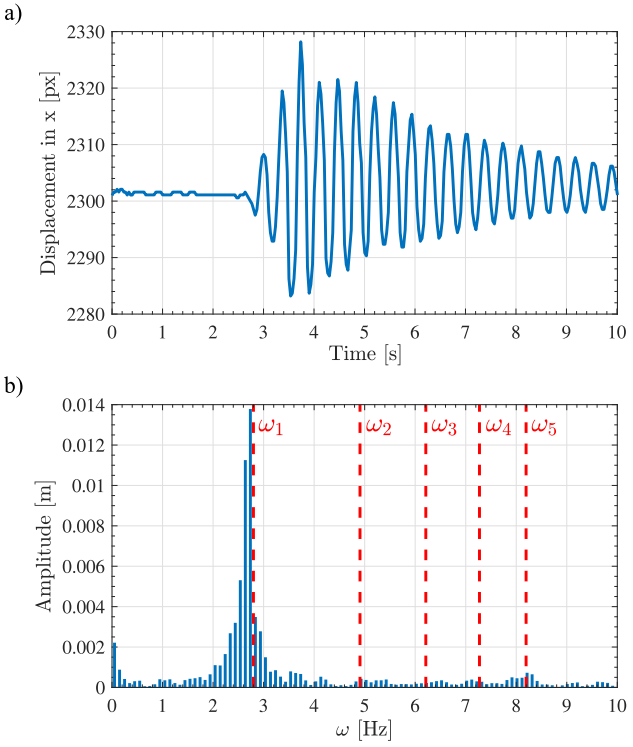

Figure 10: Evolution and Fast Fourier Transform of the raw displacement of a single laser point during a ground test. a) Time domain signal. b) Frequency domain signal and theoretical modes.

Table 3
Performance analysis of the Sloshing Detection Subsystem

ID	γ [deg]	p_{00} [m]	p_{10}	$\overline{\gamma}_X$ [deg]	p_{01}	$\overline{\gamma}_Y$ [deg]	R^2	RMSE	SSE
1	0	4.99e-2	1.084e-2	0.62	-3.33e-3	-0.19	0.751	1.991e-4	6.740e-07
2	5	4.97e-2	8.478e-2	4.85	1.06e-2	0.61	0.987	3.010e-4	1.540e-06
3	10	4.94e-2	1.655e-1	9.39	2.21e-2	1.27	0.987	5.907e-4	5.932e-06
4	15	4.92e-2	2.635e-1	14.76	3.11e-2	1.78	0.990	8.234e-4	1.153e-05
5	20	4.89e-2	3.708e-1	20.35	4.52e-2	2.58	0.989	1.178e-3	2.360e-05
6	25	4.87e-2	4.932e-1	26.25	5.91e-2	3.38	0.989	1.568e-3	4.179e-05
7	30	4.84e-2	6.085e-1	31.32	7.45e-2	4.26	0.989	1.923e-3	6.288e-05
8	35	4.80e-2	7.457e-1	36.71	8.85e-2	5.06	0.989	2.419e-3	9.950e-05
	-	**4.90e-2**	-	-	-	-	**0.959**	**1.125e-3**	**3.093e-05**

Figure 10 shows the free oscillatory movement of a single laser point in the x axis and the Fast Fourier Transform of the centered signal. Measurements are taken in normal gravity conditions with 5 cm of ferrofluid filling the 11 cm diameter cylindrical container. The red lines in the frequency domain represent the theoretical lateral sloshing frequencies, computed by means of classical normal-gravity expressions [2]. The fundamental mode is predominant and matches the predictions. Higher order modes are less prominent, but also seem to be represented by the frequency spectrum. The logarithmic decrement of the oscillation (and hence the fundamental damping ratio) can be easily extracted from either the time (exponential fitting) or frequency domain (half-power bandwidth) signals. This value is affected by the image distortion produced by the camera, but the effect is assumed to be negligible for small oscillations.

5. Conclusions

In this work, a novel method to reconstruct the free surface of an opaque liquid inside a tank has been presented. The result is an inexpensive, compact, and accurate sloshing detection system. The device has been designed to satisfy the technical and scientific requirements of the 2019 UNOOSA DropTES experiment StELIUM, launched at ZARM's drop tower in November 2019.

The detection system is able to reconstruct the free liquid surface and measures the sloshing frequencies and damping ratios by correlating the projection of a laser pattern with camera measurements. Redundant observations of the natural frequencies are obtained with a time-of-flight sensor while inertial data are collected with an accelerometer. The 3D-printed structure maintains the mechanical integrity under highly demanding conditions and ensures a smooth adaptation to different tank geometries. A high operational autonomy is achieved by means of Arduino-based electronics, which also provide a simple and robust interface with the capsule control system.

The ideal resolution of the pointer-based system ranges between 0.8 mm/px and 0.3 mm/px with the proposed configuration. However, geometrical and post-processing factors reduce the accuracy of the system, leading to errors between $\pm$0.2 mm and $\pm$2.4 mm depending on the elevation of the surface. An accurate camera calibration and geometrical definition becomes paramount for improving the performance of the system. Nevertheless, the lateral sloshing frequencies and damping ratios of the liquid can be obtained with high accuracy from the movement of a single laser diode.

From the systems engineering viewpoint, the high-level requirements listed Tab. 1 are satisfied with the proposed design. The low cost of the detection setup justifies a non-optimal solution, which in any case can be corrected with static liquid level measurements. The method here presented may be extended to transparent liquids by making use of a polarizer and a non-penetrating laser frequency band. Several space applications dealing with the management of liquids may consequently benefit from this approach.

Competing Interests

The authors declare no competing interests.

Funding Sources

This work was supported by the United Nations Office for Outer Space Affairs (UNOOSA), the Center of Applied Space Technology and Microgravity (ZARM) and the German Space Agency (DLR) in the framework of the UNOOSA DropTES Programme 2019. Further financial and academic support was obtained from Ferrotec Corporation, Politecnico di Milano, the University of Seville, the European Space Agency (ESA) and the European Low Gravity Research Association (ELGRA).

Acknowledgements

The authors acknowledge the financial, technical and academic support offered by UNOOSA, DLR, ZARM, Ferrotec Corporation, Politecnico di Milano and the University of Seville. We also thank ESA and ELGRA for financing the presentation of this work at the 70th International Astronautical Congress (IAC) and the 26th ELGRA Biennial Symposium and General Assembly. This project is in debt with ZARM's drop tower engineers Jan Siemer and Fred Oetken, ZARM's point of contact Dr Thorben Könemann and UNOOSA's point of contact Ayami Kojima for their endless

support. We finally would like to thank the technicians Giovanni Colombo, Alberto Verga and the PhD student Riccardo Bisin from the Space Propulsion Laboratory (SPLab) of Politecnico di Milano for their academic and technical assistance, as well as the rest of members of this research group for contributing to the creation of an extraordinary professional and human environment.

References

[1] W. C. Reynolds, H. M. Satterlee, The Dynamic Behavior of Liquids in Moving Containers, NASA SP-106, 1966.

[2] F. Dodge, The New Dynamic Behavior of Liquids in Moving Containers, Southwest Research Institute, San Antonio, TX, 2000.

[3] F. T. Dodge, L. R. Garza, Simulated low-gravity sloshing in spherical, ellipsoidal, and cylindrical tanks, Journal of Spacecraft and Rockets 7 (2) (1970) 204–206.

[4] K. Ohno, M. Shimoda, T. Sawada, Optimal design of a tuned liquid damper using a magnetic fluid with one electromagnet, Journal of Physics: Condensed Matter 20 (20) (2008) 204146.

[5] T. Sawada, Y. Ohira, H. Houda, Sloshing motion of a magnetic fluid in a cylindrical container due to horizontal oscillation, Energy Conversion and Management 43 (3) (2002) 299–308.

[6] F. T. Dodge, L. R. Garza, Free-surface vibrations of a magnetic liquid, Journal of Engineering for Industry 94 (1) (1972) 103–108.

[7] T. Sawada, S. Shibata, Y. Matsubara, H. Kikura, T. Tanahashi, Liquid sloshing of a magnetic fluid in a rectangular container, Nihon Kikai Gakkai Ronbunshu, B Hen/Transactions of the Japan Society of Mechanical Engineers, Part B 60 (572) (1994) 1250–1255.

[8] F. T. Dodge, L. R. Garza, Experimental and Theoretical Studies of Liquid Sloshing at Simulated Low Gravity, Journal of Applied Mechanics 34 (3) (1967) 555–562.

[9] T. Coney, J. Salzman, Lateral sloshing in oblate spheroidal tanks under reduced- and normal-gravity conditions, Tech. Rep. TN D-6250, NASA (1971).

[10] S. Sudo, H. Hashimoto, A. Ikeda, K. Katagiri, Some studies of magnetic liquid sloshing, Journal of Magnetism and Magnetic Materials 65 (2) (1987) 219 – 222.

[11] N. Ramachandran, F. Leslie, P. Peters, R. Sisk, A novel method of gradient forming and fluid manipulation in reduced gravity environments, in: 36th AIAA Aerospace Sciences Meeting and Exhibit, 1998, AIAA Paper 1998-733.

[12] J. G. Marchetta, A. P. Winter, Simulation of magnetic positive positioning for space based fluid management systems, Mathematical and Computer Modelling 51 (9) (2010) 1202 – 1212.

[13] R. Zhou, M. Vergalla, S. Chintalapati, D. Kirk, H. Gutierrez, Experimental and numerical investigation of liquid slosh behavior using ground-based platforms, Journal of Spacecraft and Rockets 49 (6) (2012) 1194–1204.

[14] J. Martin, J. Holt, Magnetically actuated propellant orientation experiment, controlling fluid motion with magnetic fields in a low-gravity environment, Tech. Rep. TM-2000-210129, M-975, NAS 1.15:210129, NASA (2000).

[15] G. Lapilli, D. Kirk, H. Gutierrez, P. Schalhorn, B. Marsell, J. Roth, J. Moder, Results of microgravity fluid dynamics captured with the spheres-slosh experiment, in: Proceedings of the 66th International Astronautical Congress, Jerusalem, Israel, 2015.

[16] Y. Takeda, Velocity profile measurement by ultrasound doppler shift method, International Journal of Heat and Fluid Flow 7 (4) (1986) 313–318.

[17] T. Sawada, H. Kikura, T. Tanahashi, Kinematic characteristics of magnetic fluid sloshing in a rectangular container subject to non-uniform magnetic fields, Experiments in Fluids 26 (3) (1999) 215–221.

[18] T.-H. Wang, M.-C. Lu, C.-C. Hsu, C.-C. Chen, J.-D. Tan, Liquid-level measurement using a single digital camera, Measurement 42 (4) (2009) 604 – 610.

[19] Y. Miao, S. Wang, Small amplitude liquid surface sloshing process detected by optical method, Optics Communications 315 (2014) 91 – 96.

[20] H. Zhang, S. Han, S. Liu, S. Li, L. Ji, X. Zhang, 3D shape reconstruction of large specular surface, Appl. Opt. 51 (31) (2012) 7616–7625.

[21] L. Huang, C. S. Ng, A. K. Asundi, Fast full-field out-of-plane deformation measurement using fringe reflectometry, Optics and Lasers in Engineering 50 (4) (2012) 529 – 533.

[22] Y. Ding, F. Li, Y. Ji, J. Yu, Dynamic fluid surface acquisition using a camera array, in: 2011 International Conference on Computer Vision, Barcelona, Spain, 2011.

[23] J. Ye, Y. Ji, F. Li, J. Yu, Angular domain reconstruction of dynamic 3d fluid surfaces, in: 2012 IEEE Conference on Computer Vision and Pattern Recognition, Providence, RI, USA, 2012.

[24] S. Thapa, N. Li, J. Ye, Dynamic fluid surface reconstruction using deep neural network, in: 2020 IEEE/CVF Conference on Computer Vision and Pattern Recognition (CVPR), 2020, pp. 21–30.

[25] A. Simonini, R. Theunissen, A. Masullo, M. R. Vetrano, Piv adaptive interrogation and sampling with image projection applied to water sloshing, Experimental Thermal and Fluid Science (2019) 559–574.

[26] J. Park, S. Im, H. J. Sung, J. S. Park, Piv measurements of flow around an arbitrarily moving free surface, Experiments in Fluids 56 (3) (2015).

[27] Y. Qian, M. Gong, Y. Yang, Stereo-based 3d reconstruction of dynamic fluid surfaces by global optimization, in: 2017 IEEE Conference on Computer Vision and Pattern Recognition (CVPR), Honolulu, HI, USA, 2017.

[28] L. Chatellier, S. Jarny, F. Gibouin, L. David, A parametric piv/dic method for the measurement of free surface flows, Experiments in Fluids 54 (3) (2013) 1488.

[29] C. H. Chien, T. H. Su, C. J. Huang, Y. J. Chao, W. L. Yeh, P. S. Lam, Application of digital image correlation (dic) to sloshing liquids, Optics and Lasers in Engineering 115 (2019) 42 – 52.

[30] A. Romero-Calvo, F. Maggi, H. Schaub, Prospects and challenges for magnetic propellant positioning in low-gravity, in: Proceedings of the AAS Guidance, Navigation and Control Conference, Breckenridge, Colorado, 2020, pp. 497–515.

[31] J. Marchetta, J. Hochstein, Fluid capture by a permanent ring magnet in reduced gravity, in: 37th Aerospace Sciences Meeting and Exhibit, 1999, AIAA Paper No. 1999-0845.

[32] J. Marchetta, J. Hochstein, Simulation and dimensionless modeling of magnetically induced reorientation, in: 38th Aerospace Sciences Meeting and Exhibit, 2000, AIAA Paper No. 2000-0700.

[33] A. Romero-Calvo, G. Cano Gómez, E. Castro-Hernández, F. Maggi, Free and Forced Oscillations of Magnetic Liquids Under Low-Gravity Conditions, Journal of Applied Mechanics 87 (2), 021010 (12 2020).

[34] A. Romero-Calvo, A. García-Salcedo, F. Garrone, I. Rivoalen, G. Cano-Gómez, E. Castro-Hernández, M. Herrada, F. Maggi, StELIUM: A student experiment to investigate the sloshing of magnetic liquids in microgravity, Acta Astronautica 173 (2020) 344 – 355.

[35] D. A. Forsyth, J. Ponce, Computer Vision: A Modern Approach, Prentice Hall Professional Technical Reference, 2002.

[36] D. Wierzbicki, Multi-camera imaging system for UAV photogrammetry, Sensors 18 (8) (2018) 2433.

[37] D. Scaramuzza, A. Martinelli, R. Siegwart, A toolbox for easily calibrating omnidirectional cameras, in: 2006 IEEE/RSJ International Conference on Intelligent Robots and Systems, Benjing, China, 2006, pp. 5695–5701.

[38] T. Luhmann, C. Fraser, H. Maas, Sensor modelling and camera calibration for close-range photogrammetry, ISPRS Journal of Photogrammetry and Remote Sensing 115 (2016) 37 – 46.

[39] F. Remondino, C. Fraser, Digital camera calibration methods: Considerations and comparisons, in: ISPRS Commission V Symposium 'Image Engineering and Vision Metrology', Dresden, Germany, 2006.

[40] J. Bouget, Camera calibration toolbox for Matlab, accessed: 2019-09-12 (2019).
URL http://www.vision.caltech.edu/bouguetj/calib_doc/

[41] D. T. Operation, S. Company, ZARM Drop Tower User Manual, ZARM FABmbH, 2011.

[42] A. Romero-Calvo, I. R. A. J. García-Salcedo, F. Garrone, E. C.-H. G. Cano-Gómez, F. Maggi, Free surface reconstruction of opaque liquids in microgravity. Part 2: results of drop tower campaign, Acta Astronautica (2020).